Impact of Laser Texturing on Ni-Based Single Crystal Superalloys

Lucille Despres, Sophie Costil, Jonathan Cormier, Patrick Villechaise, Romain Cariou

metals

MDPI

Article

Impact of Laser Texturing on Ni-Based Single Crystal Superalloys

Lucille Despres [1,2], Sophie Costil [1,*], Jonathan Cormier [3], Patrick Villechaise [3] and Romain Cariou [2]

[1] Laboratoire Interdisciplinaire Carnot de Bourgogne, Université de Bourgogne Franche-Comté—UTBM, UMR 6303 CNRS, 90100 Belfort, France; lucille.despres@unilim.fr
[2] Plateforme Aubes de Turbine Avancées, Safran Tech, 92230 Gennevilliers, France; romain.cariou@safrangroup.com
[3] Département de Physique et Mécanique des Matériaux, Institut P', 1, Avenue Clément ADER BP 40109, 86961 Chasseneuil du Poitou, France; jonathan.cormier@ensma.fr (J.C.); patrick.villechaise@ensma.fr (P.V.)
* Correspondence: sophie.costil@utbm.fr

Abstract: Surface laser texturing is used to ensure mechanical anchoring and strengthen adhesion between the interfaces of bond coatless thermal barrier coating system. To anticipate a possible loss of mechanical properties and to adapt to the perpetual evolutions of chemical compositions of the system, we analyzed the microstructural evolutions of different Ni-based single crystal superalloys, induced during infrared nanosecond laser ablation. Localized asperities composed of a melted, re-solidified matter, with a different microstructure from that of the bulk material, were generated. Regarding asperity morphologies, recrystallization within the latter could be avoided. Then, to compare different Ni-base single crystal superalloys, the thermal-affected volumes were characterized for two patterns textured under different energetic conditions. It seems that all the studied single crystal superalloys behaved quite similarly during nanosecond laser ablation. Finally, according to these results, ablation kinetics between the γ and γ' phases of Ni-based superalloys could not be homogeneous.

Keywords: laser texturing; superalloys; microstructure

Citation: Despres, L.; Costil, S.; Cormier, J.; Villechaise, P.; Cariou, R. Impact of Laser Texturing on Ni-Based Single Crystal Superalloys. *Metals* **2021**, *11*, 1737. https://doi.org/10.3390/met11111737

Academic Editor: Alexandre Emelyanenko

Received: 4 October 2021
Accepted: 26 October 2021
Published: 30 October 2021

1. Introduction

To meet environmental challenges, it is necessary to reduce fuel usage and NOx and CO/CO_2 emissions of aero-engines. Land-based gas turbines are developed to increase the turbine efficiency while lowering the production costs [1,2]. Consequently, the recent development of an internal cooling network in HP turbine blades coupled with the use of a thermal barrier coating allows an increase in the turbine entry temperature [3–5]. A thermal barrier coating system is usually composed of three different layers, a bond coat, a natural oxide layer called TGO (Thermally Grown Oxide) and a ceramic top coat, deposited onto a nickel-based single crystal superalloy.

In service, the components of the hottest part of the engines are submitted to complex loadings: creep, thermomechanical fatigue and oxidation at high temperature, which could be deleterious for the TBC system durability and could lead to a premature spallation of the top coat [6]. The critical damage mechanisms of the TBC system are mainly related to the coupled evolution of the TGO and the bond coat [7]. These evolutions are due to the growth of the TGO by oxidation [8], and the deformation of TGO/bond coat interface by ratcheting [7] or rumpling [9], in order to relax the accumulated stresses [7,10–16].

To overcome the damage mechanisms localized close to the bond coat and thus slow down the spallation of the top coat, studies have been carried out to develop bond coatless thermal barrier coating system [17–19]. Laser surface texturing strengthens the adhesion

between the superalloy and the ceramic layer, usually ensured by the bond coat, without any surface contamination. Indeed, mechanical anchoring is often favored by strong roughness at the interface between an adhesive and its substrate [20,21]. Therefore, controlling the superalloy surface morphology by laser texturing seems to be a promising alternative to a sand blasted bond coat. The benefits of this surface treatment on the coating adhesion mechanisms are well known [22–28]. Kromer et al. showed that laser surface texturing promotes better adhesion during creep and thermal fatigue solicitations than sandblasting surface for a zirconia partially stabilized by yttria top coat deposited on AM1 by air plasma spray. Indeed, cavities surrounded by melted/re-solidified matter increase surface roughness, strengthening mechanical anchoring, which avoids a premature spallation of the top coat. Moreover, these authors demonstrate that the crack propagation interface leading to spallation of the TBC is clearly deviated by surface patterns [19].

To follow these researchers and to respond to the perpetual evolution of the single crystal superalloy compositions essentially developed to increase the creep resistant of turbine blades [3,29–32], we aim with this study to analyze the behavior of different single crystal superalloys via laser ablation by nanosecond infrared laser. Apart from some authors who mainly studied the behavior of superalloys via ultra-shot pulse duration (picosecond or femtosecond) laser ablation [33–37], different superalloys have never been compared. Moreover, nanosecond laser ablation seems to be the most relevant ablation regime in order to generate rougher surfaces with the asperity formation around cavities [38,39], increasing mechanical anchoring and slowing down crack propagation [40]. Finally, to anticipate the superalloy prospective loss of mechanical properties, it is important to study the possible damage mechanisms, close to the cavities, induced during laser interaction. This way, after exploring the surface morphologies induced by laser treatments, the influence of the superalloy microstructures and cavity morphologies during the laser ablation process are discussed.

2. Materials and Methods

2.1. Materials and Heat Treatments

This study was carried out using Ni-based single crystal superalloys (first, second and third generation). The compositions of these Ni-based superalloys, casted using a standard Bridgman process, are given in Table 1.

Table 1. Chemical compositions of the studied Ni-based single crystal superalloys.

Alloy	Solvus	Density (g/cm3)	Composition (wt.%)								
			Ni	Co	Cr	Mo	W	Ta	Al	Ti	Re
AM1	1268 +/− 5	8.59	Bal.	6.5	7.8	2.0	5.7	7.9	5.2	1.1	/
CMSX-4	1293 +/− 7	8.7	Bal.	9.7	6.4	0.6	6.4	6.5	5.6	1.1	2.9
CMSX-4 Plus	1334 +/− 5	8.93	Bal.	10.0	3.5	0.6	6.0	8.0	5.7	0.9	4.8
MAR M200 + Hf	1205 −/+ 10	8.61	Bal.	9.5	8.6	-	11.8	-	4.9	1.9	-
MC2	1265 +/− 5	8.63	Bal.	5.0	8.0	2.0	8.0	6.0	5.0	1.5	-

The behavior of different Ni-based single crystal superalloys and the influence of superalloy microstructures during the laser ablation process were evaluated. It is well known that solution heat treatments confer a classical γ/γ' microstructure. Additional aging treatments allow us to obtain a cuboidal morphology with γ'-precipitates having an average 0.4–0.5 μm edge length. Figure 1 shows an example of the influence of aging treatments applied after solution heat treatment on the microstructure of a first generation Ni-based single crystal superalloy (AM1). The different heat treatments applied are given in Table 2.

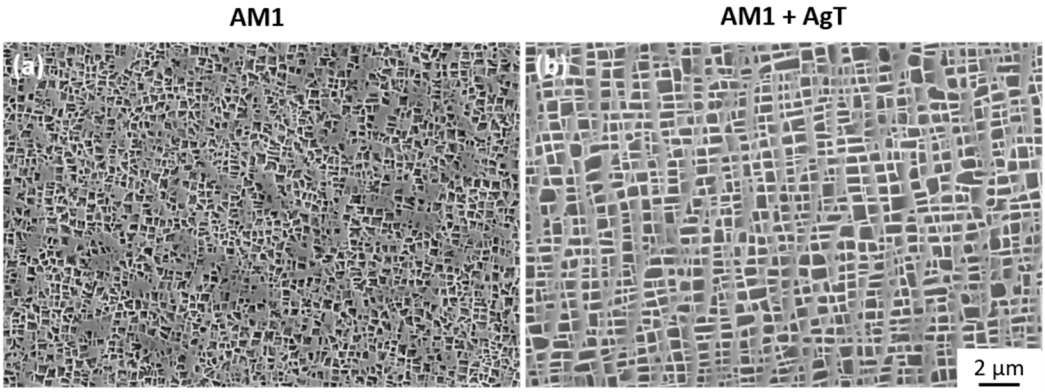

Figure 1. Example of the Ni-based single crystal superalloy microstructures (AM1 here) after (**a**) solution heat treatment, (**b**) aging treatments.

Table 2. Applied solution and aging heat treatments.

Alloy	Solution Heat Treatment	Aging Treatment
AM1	1300 °C/3 h/AQ	1100 °C/5 h/AQ + 870 °C/16 h/AQ
CMSX-4	1277 °C/2 h + 1288 °C/2 h + 1296 °C/3 h + 1304 °C/3 h + 1313 °C/2 h + 1316 °C/2 h + 1318 °C/2 h + 1321 °C/2 h/GFC	1140 °C/6 h/AQ + 871 °C/20 h/AQ
CMSX-4 Plus	1313 °C/2 h + 1318 °C/2 h + 1324 °C/6 h + 1335 °C/6 h/GFC	1163 °C/6 h/AQ + 871 °C/20 h/AQ
MAR M200 + Hf	1210 °C/0.5 h + 1225 °C/0.5 h + 1240 °C/4 h/AQ	1100 °C/5 h/AQ + 870 °C/16 h/AQ
MC2	1300 °C/3 h/AQ	1080 °C/6 h/AQ + 870 °C/16 h/AQ

All the superalloys studied have received at least their corresponding solution heat treatments. Some were also treated by additional aging treatments and were named for the following by the suffix "+AgT" (as mentioned in Figure 1).

Moreover, it is well known that the γ′-precipitates morphology is fully dependent on the thermal history of the material [41]. So, in order to evaluate the influence of various superalloy microstructures during laser ablation, samples of AM1 and MAR M200 + Hf were water quenched, air quenched or gas furnace cooled after solution heat treatments. Indeed, the γ′-precipitate size is controlled by cooling rate.

Finally, to bring additional information on the ablation mechanisms of Ni-based superalloys, pure nickel and polycrystalline Ni-based superalloy Inconel 718 were studied. Both materials are devoid of the γ′ phase (less than 5% for the Inconel 718). Table 3 gives the chemical composition of the Inconel 718 composed of γ/γ′′ morphology.

Table 3. Chemical compositions of Inconel 718.

Alloy	Density (g/cm3)	Composition (wt.%)									
		Ni	Co	Cr	Mo	Al	Ti	Nb	C	B	Fe
Inconel 718	8.19	50–55	<1	17–21	2.8–3.3	0.2–0.8	0.65–1.15	4.75–5.5	0.04	0.02	18.5

2.2. Laser Surface Treatments

Polished specimens (0.18 +/− 0.05 µm) were laser textured with a pulsed fiber laser (Laseo, Ylia M20, Quantel, France) to structure the surface [42]. The laser operated at a nominal wavelength of 1.06 µm with pulse duration of 100 ns, a maximum power of 20 W and variable frequency varying between 20 and 100 kHz. The laser beam used for this operation is circular with a diameter of 60 µm at the focal point and a gaussian energy distribution.

Laser texturing is a surface treatment based on the principle of laser ablation in pulse regime [43,44]. By focusing the laser on one spot on the surface, the accumulation of impacts, governed by the pulse frequency, allows the creation of cavities (see Figure 2) [45–

47]. The physical phenomena induced during the laser-matter interaction occur during extremely short duration which leads to a rapid solidification of the melted matter. So, some asperities around cavities, composed of re-solidified matter, could be generated after the laser ablation process [48,49]. The laser-matter interaction is highly dependent on the nature of the impacted materials and the characteristics of the used laser [50,51].

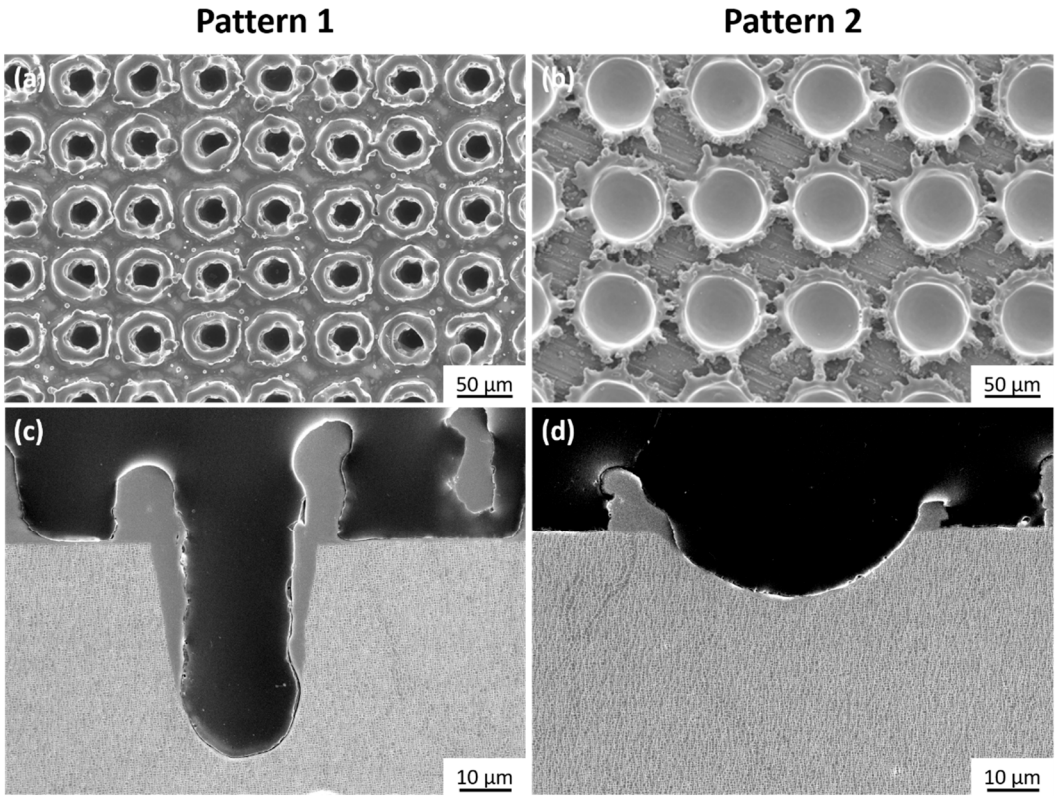

Figure 2. (**a**) Top view of pattern 1, (**b**) top view of pattern 2, (**c**) cross-section of pattern 1, (**d**) cross-section of pattern 2.

Laser patterning consists of series of equidistant lines covered with holes. Various morphologies according to the shapes, depths, diameters, asperities or even spacing between patterns could be obtained. Thus, using laser texturing, it is possible to design an infinite number of surfaces. We opted during this work to study only two specific geometries of patterns, one with larger opened cavities and the other with deeper cavities. These two patterns are designated such as:

- "Pattern 1", formed by holes spaced 60 µm apart generated by 50 pulses at a laser intensity of $8.8.10^{-2}$ GW/cm².
- "Pattern 2", formed by holes spaced 100 µm apart generated by 15 pulses at a laser intensity of $1.8.10^{-1}$ GW/cm².

These two sets of applied laser parameters (fluence, impact number) simulate two representative laser ablation regimes. Moreover, these two surface morphologies textured on the different single crystal superalloys, shown in Figure 2, could be promising candidates to increase surface roughness and strengthen mechanical anchoring. Whatever the superalloys, the patterns seem to exhibit a regular morphology with a depth and diameter equal to about 53 µm and 30 µm, respectively, for pattern 1 and 20 µm and 60 µm, respectively, for pattern 2.

2.3. Characterization Methods

Considering the laser–matter interactions and all the induced surface modifications, several characterization methods must be carried out. Due to the high cavity depths

generated, it is difficult to characterize textured surfaces by standard roughness measurement techniques. Observations from cross sections of the different textured patterns have been compared between studied superalloys. Series of preparation steps were then imposed to analyze specimens after laser treatments.

First, epoxy resin was used for the cold mounting of the sample. This step is essential to protect textured patterns and avoid any degradation during cutting and polishing. Then, samples were cut (Mecatom T210 (4500 rpm, 0.1 mm/s)) and carefully polished up to the micron, cleaned with ethanol in an ultrasonic bath for 5 min and etched using a solution of 1/3 HNO_3 + 2/3 HCl (volume part) to dissolve the γ' phase and reveal the superalloy microstructure. Finally, the samples were metallized by a nanometric layer of gold–palladium. Morphologies and microstructures were evaluated with a Scanning Electron Microscope (JEOL 6400, 7000 F, 7800 F) operating at 25 kV.

For this study, we chose to analyze the microstructure close to the generated cavities in order to understand the ablation mechanisms of Ni-based single crystal superalloys. To compare the materials, the thermally affected volumes were evaluated. For this, at least six SEM images of each textured pattern (cross sectional view), at ×1000 magnification, were processed by the ImageJ software. The considered volume is determined by the following equation:

With V (μm^3) the thermally affected volume, depth (μm) and diameter (μm) the geometrical measured dimensions. The depth and diameter considered for both textured patterns are described in Figure 3.

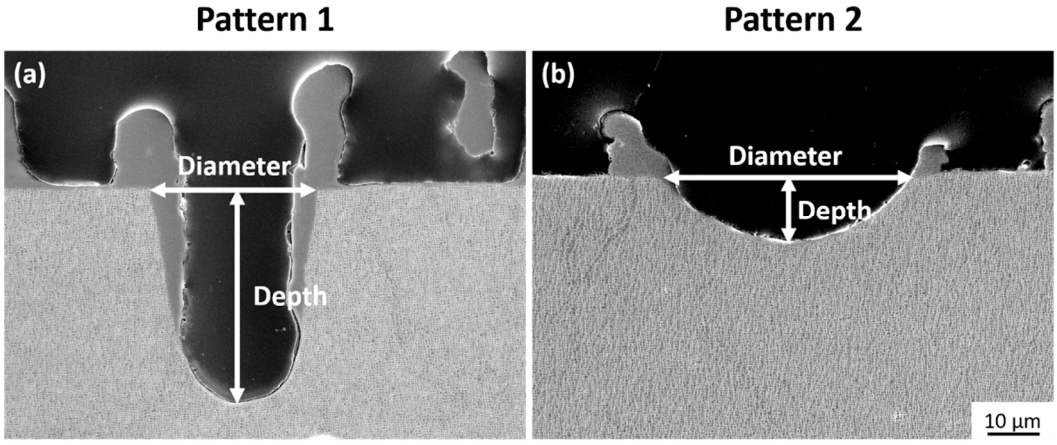

Figure 3. Dimensions considered for the thermally affected volume calculation: (**a**) pattern 1, (**b**) pattern 2.

Finally, to characterize the crystallographic orientation of the melted matter (asperities) re-solidified around the cavities, EBSD analyses were carried out using the FEG JEOL 7000 F SEM and the OIM software. All the presented maps were coded according to the z-axis, which is parallel to the solidification axis of the studied single crystal superalloys. Due to the encountered difficulties during the sample preparation, only on the sample of AM1 + AgT was analyzed. At least three cavities out of the two considered patterns were characterized.

3. Results

In order to anticipate a possible loss of the mechanical properties, it is necessary to study the single crystal superalloy microstructure after laser surface treatments. Indeed, the evolution of the γ/γ' morphology is representative of the material thermal history [41]. Consequently, it could be a relevant marker of the involved laser ablation mechanisms. The behavior of the different single crystal superalloys and the influence of its microstructures against nanosecond infrared laser ablation were analyzed.

3.1. Microstructural Evolutions Close to the Textured Patterns

As an illustration, Figure 4 shows the two patterns textured on the surface of different single crystal superalloys. The following observations were similar whatever the considered Ni-based superalloys and the applied heat treatments. The shapes including the asperity morphologies (black arrows) are fully dependent on the chosen laser parameters (fluence, impact number, etc.). These asperities composed of melted, re-solidified matter are clearly recognizable by the uniform gray color. As seen in Figure 5, the microstructure of this area is completely different from the material core. Indeed, the standard γ/γ' morphology is not observable here. This area seems to be composed of only one phase.

Figures 4c and 4d focus on the hole bottoms of patterns 1 and 2, respectively. A heat-affected area (thickness of 1.8 μm and 1.4 μm for patterns 1 and 2, respectively), where the γ'-precipitates lose their regular morphology, can be seen. Moreover, in this heat-affected area, the γ matrix channels (in light gray) appear to follow the hole concavity (white arrows). It is important to notice that this heat-affected area is quite small, whatever the considered pattern.

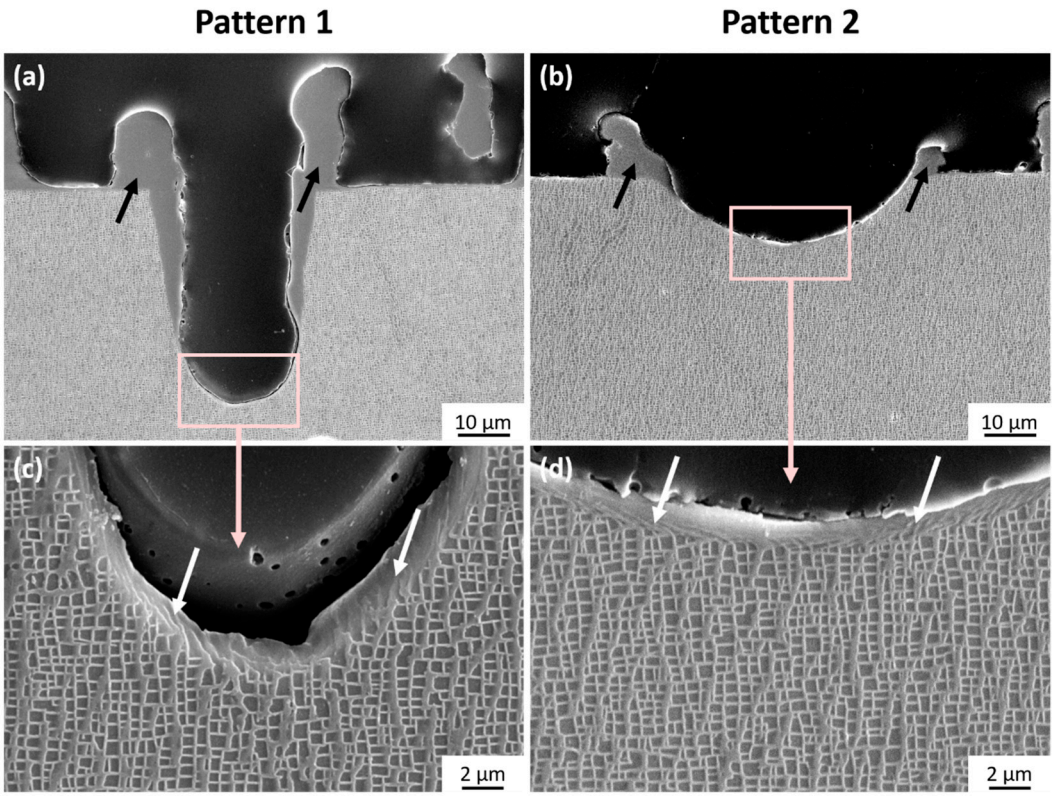

Figure 4. Microstructure of AM1 + AgT: (**a**) pattern 1, (**b**) pattern 2, (**c**) hole bottom of pattern 1 and (**d**) hole bottom of pattern 2. Black and white arrows underline generated asperities and heat-affected areas, respectively, in the hole bottoms.

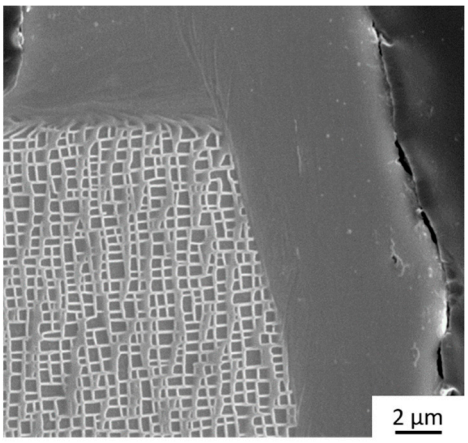

Figure 5. Magnification of AM1 + AgT microstructure close to an asperity.

The Mar M200 + Hf superalloy is the only one composed of carbides (white phases on the Figure 6). On Figure 6b, unmelted carbides within the melted, re-solidified area (asperities) can be observed.

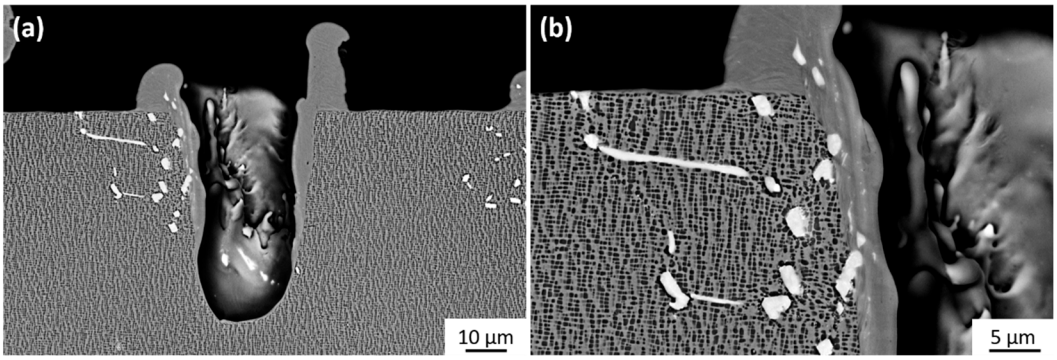

Figure 6. Non-melted carbides observed on MAR M200 + Hf + AgT specimens: (**a**) pattern, (**b**) magnification on a melted/re-solidified area.

The superalloy mechanical properties are fully dependent on the microstructure stability [52,53]. However, the asperity microstructure and probably the composition are different from those of the bulk material, which could be deleterious for the mechanical properties of the superalloys. It is relevant to analyze the solidification mechanisms of the liquid bath and to check if recrystallization occurs during the ablation of single grain superalloys. The crystallographic orientation within the asperities for both patterns was studied via EBSD analysis. Due to the difficulties of sample preparation, this study was carried out only on AM1 single crystal superalloys.

Figure 7 shows the crystallographic orientations of pattern 1. The solidification of the single crystal superalloy is close to the crystallographic orientation <001>, which appears suitable to obtain this crystallographic orientation in the core of the material. Nevertheless, only a few grains in some limited areas (revealed by the white rectangle) within asperities could be observed. Whatever the considered asperities (Figure 7c,d), it is possible to observe a color gradient characteristic of a light disorientation of the crystal lattice. The rest of the observed molten area does not show significant crystallographic disorientations.

Moreover, Figure 8 shows the EBSD mapping of pattern 2. Significant structural modifications can be observed within the melted, re-solidified asperities. First, the left asperity (Figure 8c) presents crystallographic disorientations around the asperity–superalloy junction. The most distant areas with this junction turn out to be completely

recrystallized. The right asperity (Figure 8d) is totally recrystallized. Nevertheless, elongated grains along a privileged direction parallel to the z-axis are revealed by white arrows.

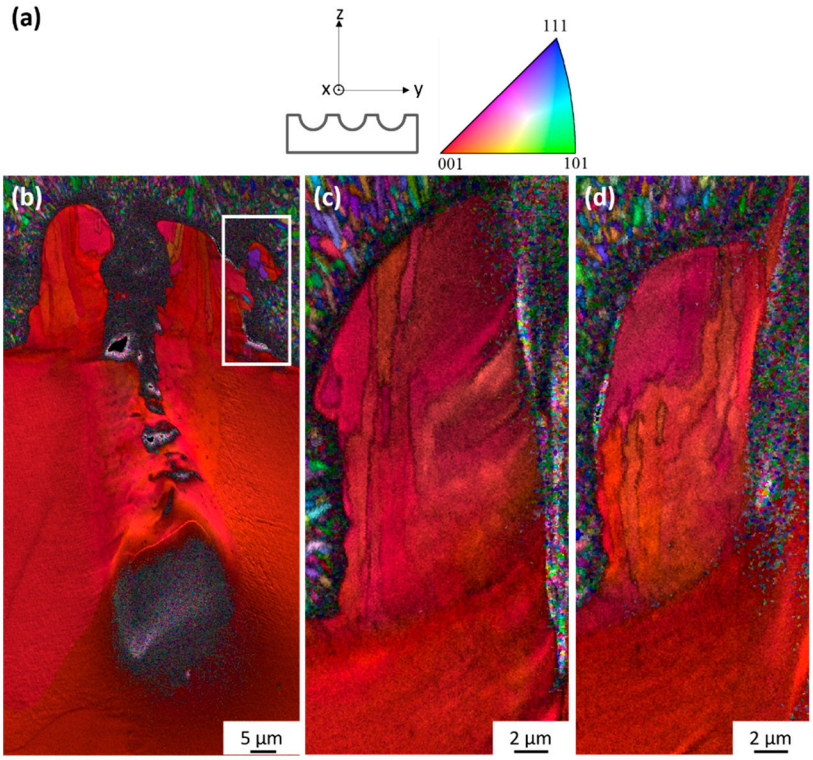

Figure 7. Crystallographic orientation mapping, coded along the z-axis of pattern 1: (**a**) reference frame and inverse pole figure (**b**) mapping of the entire pattern 1, (**c**,**d**) zoom on two different asperities. The textured surface of the AM1 was previously nickel.

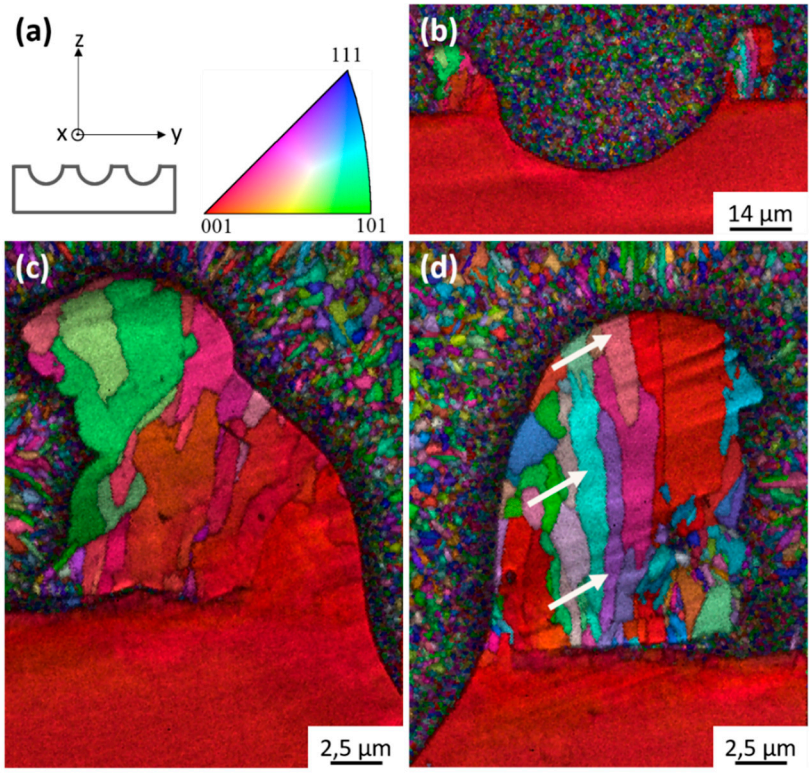

Figure 8. Crystallographic orientation mapping, coded along the z-axis, of pattern 2: (**a**) reference frame and inverse pole figure (**b**) mapping of the entire pattern 2, (**c**,**d**) zoom on both asperities. The textured surface of the AM1 was previously nickel plated.

Finally, it appears that the crystallographic orientation of the generated asperities is strongly dependent on its geometry, especially on the interface between the asperities and the bulk material. The disorientations coupled with the grain elongations along a preferential direction indicate the presence of a relatively vertical thermal gradient, close to the z-axis, within the asperities. The epitaxial growth with the substrate of some material asperities probably highlights a unidirectional displacement of the solid–liquid interface.

3.2. Comparison of Thermally Affected Volumes

The geometry of laser texturing patterns is strongly dependent on the interaction of the material with the laser beam and thus the solidification process of the material. If the geometries seemed to be relatively similar whatever the considered single crystal superalloy, we chose to focus on the thermally affected areas. The thermally affected volumes of the two patterns were approximated after laser texturing on the various single crystal superalloys. It consisted of comparing the nickel-based superalloys, and checking if the microstructural evolutions induced by the heat treatments had an impact on these volumes. Figures 9 and 10 show the obtained results for patterns 1 and 2, respectively. It appears that the heat treatments applied to optimize the microstructure of the superalloys had an influence on the thermally affected volumes after laser texturing. Indeed, considering both patterns, the volumes of AM1 and CMSX-4 Plus seem to be lower than those created on AM1 + AgT and CMSX-4 Plus + AgT, respectively. This trend seems to be reversed for the MAR M200 + Hf superalloy.

Considering only the samples which received the additional heat treatments (+AgT samples), it appears that MAR M200 + Hf + AgT behaved differently compared to the other superalloys. Indeed, for both patterns, the thermally affected volumes of MAR M200 + Hf + AgT were much smaller.

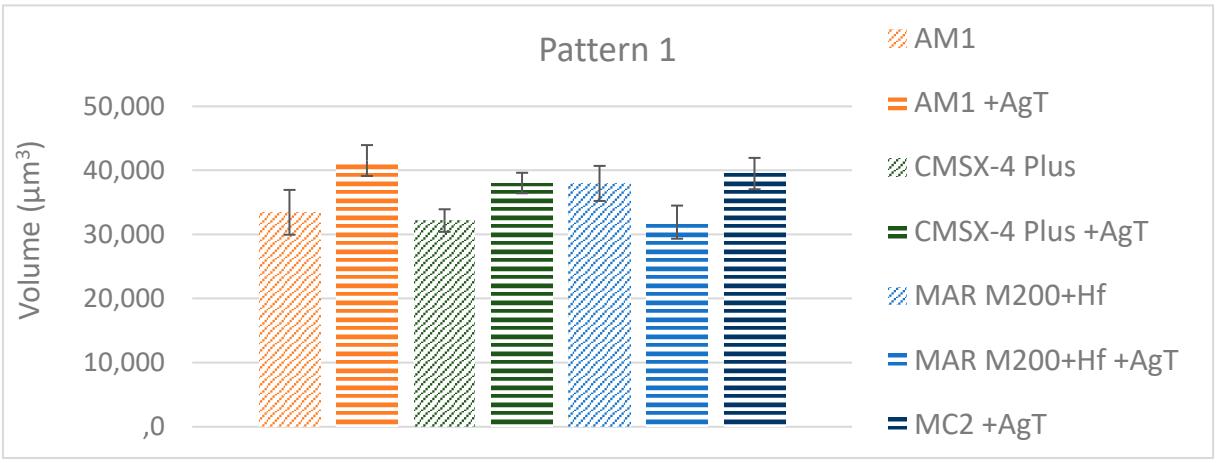

Figure 9. Thermally affected volumes of textured pattern 1 on different Ni-based single crystal superalloys.

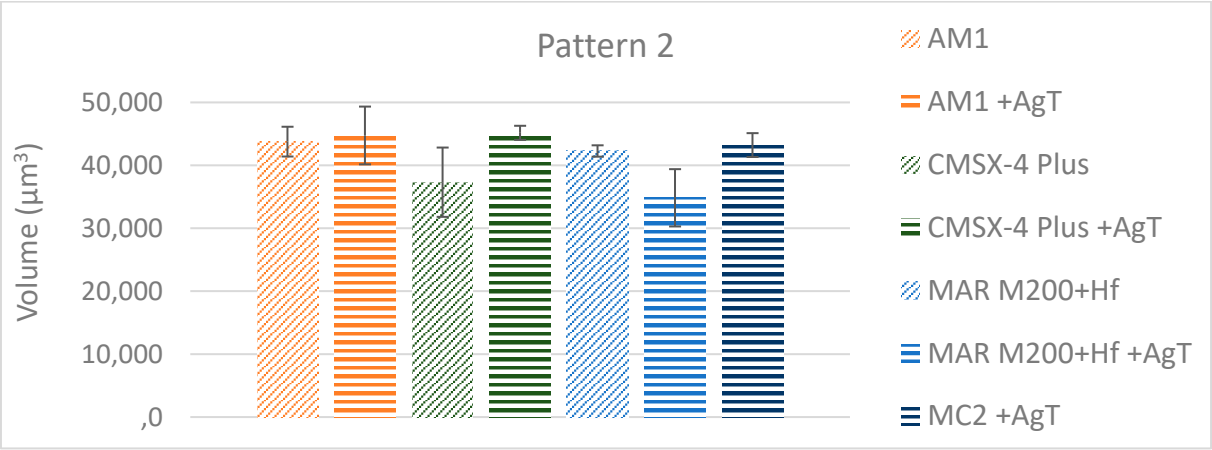

Figure 10. Thermally affected volumes of textured pattern 2 on different Ni-based single crystal superalloys.

The additional heat treatments applied after the standard solution heat treatments, which mainly promote the growth of γ′-precipitates, seem to have had an effect on the affected volume. Using an image analysis software, the size of the γ′-precipitates could be estimated (Table 4). These results show that the additional heat treatments effectively led to the coarsening of the γ′-precipitates. It is then interesting to evaluate the influence of the size of the γ′-precipitates on the affected volumes of superalloys.

Table 4. Image analysis measurements of the equivalent diameter of γ′-precipitates.

Heading	MAR M200 + Hf	MAR M200 + Hf + AgT	AM1	AM1 + AgT	CMSX4 Plus	CMSX4 Plus + AgT
Dendrite	<100 nm	~300 nm	~295 nm	~375 nm	~610 nm	~635 nm
Interdendritic area	<100 nm	~345 nm	~315 nm	~380 nm	~625 nm	~650 nm

Grosdidier et al. showed that the cooling rate after a 30 min solution heat treatment in the γ-domain of superalloys had an influence on the precipitation of the γ′ phase [41]. Similarly, Steuer et al. showed that the higher cooling rates after solution treatment of AM3, the larger γ′-precipitates [54]. To vary the precipitate size, samples of AM1 and MAR M200 + Hf were cooled at different rates after the solution heat treatments.

Figure 11 shows the microstructures of AM1 in the dendrite core based on various cooling rates applied after the solution treatment at 1300 °C. We found that a water quench, which corresponds to the fastest cooling rate, favored the formation of the finest γ′-precipitates, (Figure 11a) with an equivalent diameter that does not exceed 155 nm. The largest γ′-precipitates with an equivalent diameter close to 390 nm were obtained after cooling the sample in the furnace (Figure 11c). An air quench provided to the γ′-precipitates an equivalent diameter close to 300 nm (Figure 11b). The precipitates within the MAR M200 + Hf were much smaller than those formed in the AM1. Unfortunately, it could not be precisely characterized by image analysis. It was also difficult to make relevant measurements for the AM1 cooled by a water quench.

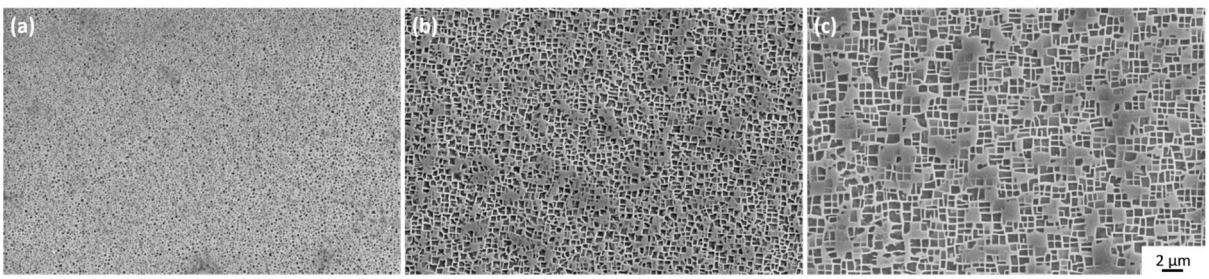

Figure 11. Microstructure of AM1 in dendrite core after solution treatment followed by: (**a**) a water quench, (**b**) an air quench and (**c**) a gas furnace cooling.

Figures 12 and 13 represent the thermally affected volumes of patterns 1 and 2, respectively, based on the sample cooling rates (water, air, furnace). Whatever the considered specimen, an evolution of the thermally affected volumes was noticed. Nevertheless, contrary to the previously observed results, it appears that the samples with the finest γ′-precipitates promoted the largest thermally affected volumes. Nevertheless, according to the obtained standard deviations, a certain overlapping of the results can be noted. This tends to minimize the real effect of the superalloy microstructure over the ablation process.

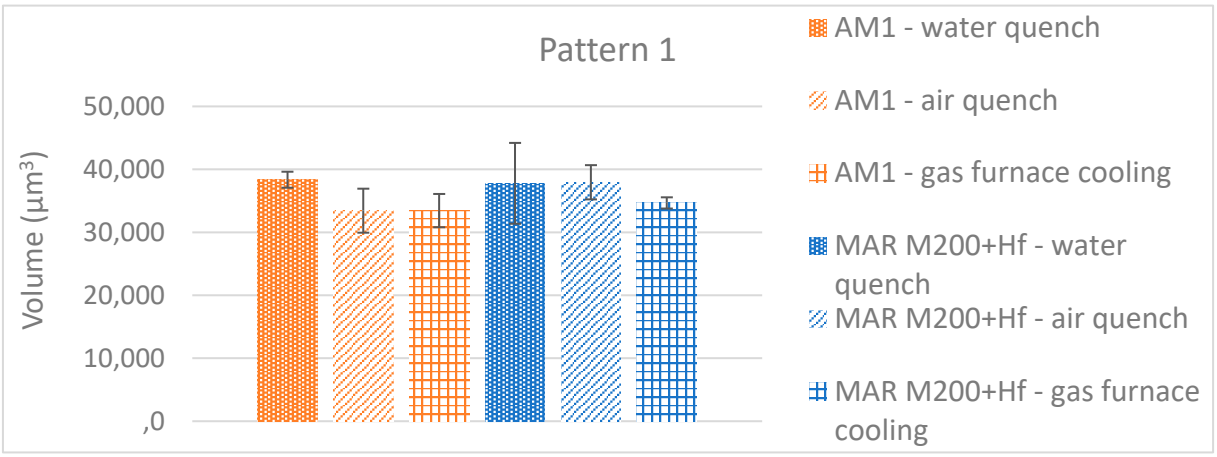

Figure 12. Thermally affected volumes of textured pattern 1 on AM1 and MAR M200 + Hf as a function of cooling kinetics.

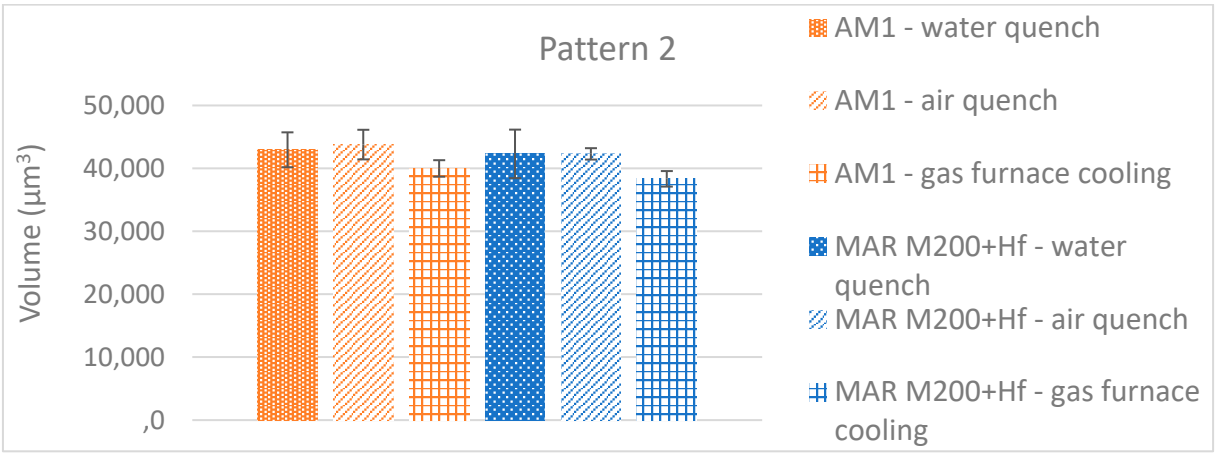

Figure 13. Thermally affected volumes of textured pattern 2 on AM1 and MAR M200 + Hf as a function of cooling kinetics.

4. Discussion

Many morphologies can be developed by laser surface texturing. For this study, we chose to study two specific morphologies (patterns 1 and 2) generated under different energetic conditions. After cross-sectional observations of these two patterns, areas composed by melted, re-solidified matter were easily observed along the cavities and on the surface in the form of asperities. The microstructure of these areas was different from that of the superalloy core. Indeed, the standard γ/γ′ morphology was not visible. Moreover, the characteristic uniform color of the asperities could show that it was probably composed by only one phase. These observations are similar regardless of the observed material. However, a variation in the amount of re-solidified matter regarding laser parameters

(energy and repetition rate) can appear. The induced energy accumulation can lead to different volumes of thermally affected material.

A microstructural transition at the bottom of the cavities was observed. Indeed, the γ′-precipitates lost their cuboidal morphology and it appeared that the γ-matrix channels followed the pattern concavities, as underlined by the white arrows in Figure 14. During laser ablation, the impact accumulation on the surface led to melting and vaporization of the material. The interaction with the laser and the vapor generated a plasma which exerts a recoil pressure on the melted matter. These physical phenomena induced a hydrodynamic flow of the liquid bath, which led to asperities [46–49]. Moreover, it seems that the γ-matrix channels followed this flow of matter.

Finally, beyond the thermally affected area, the superalloy microstructure seemed to be unaffected by the laser treatment. Indeed, the size and the morphology of the γ′-precipitates remained unchanged compared to the material core.

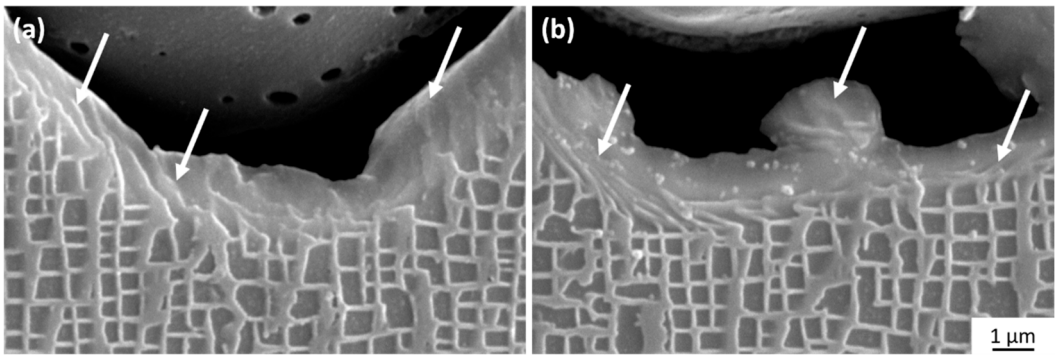

Figure 14. Microstructure at the bottom holes of two patterns 1 textured on AM1 + AgT.

EBSD analysis were carried out to characterize the generated asperities which present a different microstructure from the bulk material. The first results seemed to show a correlation between a possible recrystallization of the asperities and its geometry. Indeed, an important asperity/superalloy junction (pattern 1) favors an epitaxial growth with the substrate. On the contrary, a small junction promotes the formation of recrystallized asperities (pattern 2). Moreover, it appears that the crystallographic disorientations coupled with the grain elongations along a preferential direction indicated the presence of a relatively vertical thermal gradient, close to the z-axis, within the asperities.

To strengthen these results, the crystallographic orientation of another pattern textured on single crystal superalloy AM1 was characterized by EBSD analysis (Figure 15). The latter presented on Figure 15b was formed by holes spaced 100 µm apart generated by 40 pulses at a laser intensity of 1.7×10^{-2} GW/cm². The asperities had a spherical shape, and the asperity/superalloys junction was quite large. Figure 15c exhibits the crystallographic orientations of the material asperities of this third pattern. The color in the material core indicated that the cutting axis of the sample was not perfectly parallel to the solidification axis of the single crystal superalloy. No recrystallized grains could be observed here. Moreover, the color gradient within the asperities seemed to be insignificant, which could show an epitaxial solidification of the liquid bath with the substrate. The previous findings are therefore confirmed.

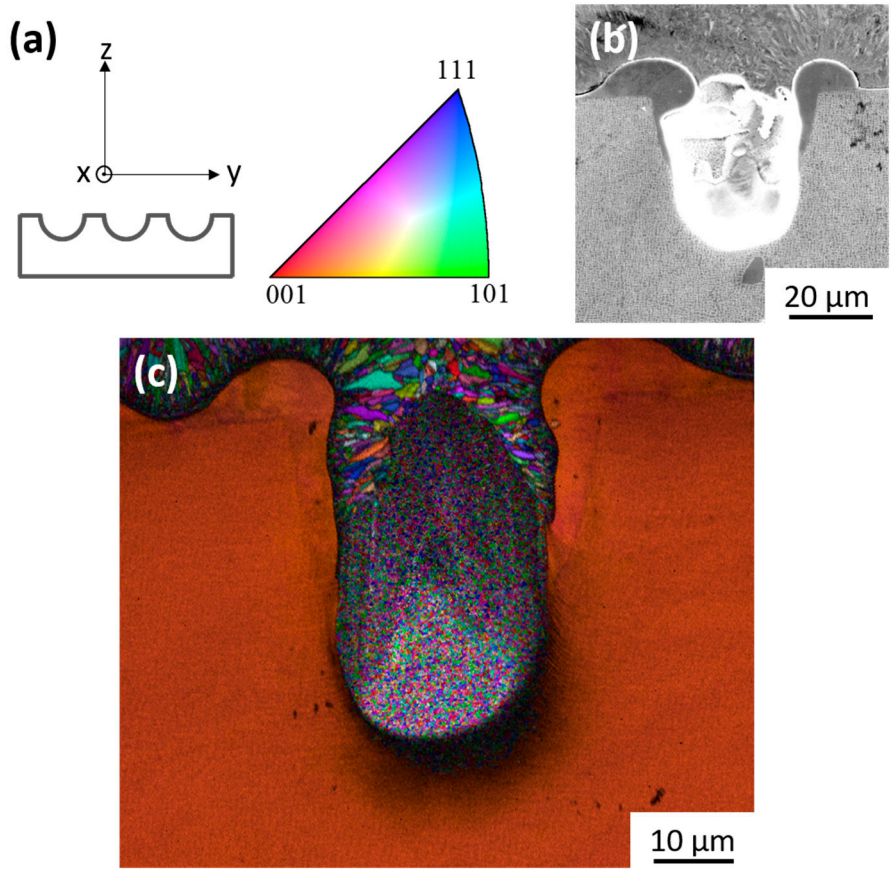

Figure 15. Crystallographic orientation mapping, coded along the z-axis: (**a**) reference frame and inverse pole figure, (**b**) morphology of the considered pattern, (**c**) mapping of the entire pattern. The textured surface of the AM1 was previously nickel plated.

During the laser texturing process, the extreme treated surface was in contact with the ambient air. The asperities were thus cooled by thermal convection. In addition, the exchanges between the liquid bath and the rest of the material also induced a cooling of the asperities by conduction. This competition in the cooling mechanisms during laser ablation promoted thermal gradients and, consequently, different solidification mechanisms. A larger asperity/superalloy junction favors a cooling by thermal conduction, which facilitates the solidification of the asperities in epitaxy with the superalloy.

After nanosecond infrared laser ablation of Ni-based single crystal superalloy AM1, Kromer et al. showed by nanoindentation that the melted, re-solidified area presented a higher Young's modulus and hardness than the superalloy core [18]. According to the author, such disparities can be explained either by the recrystallization of the melted, re-solidified area, by a nano γ'-precipitation due to high cooling rates or by the generation of dislocations due to thermal stresses induced during the solidification of the liquid bath. The presented results strengthen the hypothesis that the increase in Young's modulus and hardness are linked to the recrystallization mechanisms.

Finally, it is important to notice that laser texturing does not necessarily lead to recrystallization within the solidified material. Adjusting laser parameters could then be interesting to avoid any recrystallization which could be harmful for the material performances at high temperatures.

All the studied superalloys presented similar pattern morphologies, but to go further in the comparison of the superalloys after laser ablation, the thermally affected volumes were measured. Such dissimilarities were noticed and can be due to the differences in optical (absorption coefficient) or physical (thermal conductivity, temperature of solvus and liquidus) properties of the superalloys. For example, laser ablation is strongly

dependent on the optical properties of the materials. However, the absorption coefficients measured at ambient temperature, which reflect the amount of energy absorbed by the material, could not be correlated clearly with the thermal-affected volumes of the superalloys [28]. During this study, it was not possible to dissociate all of the material intrinsic properties.

Moreover, it seems that the same single crystal superalloys, but having different microstructures linked to the different applied heat treatments, reacted differently during the laser ablation (the thermally affected volumes are different). We therefore wonder to what extent the microstructure can have an influence on the ablation mechanisms of superalloys. Nevertheless, according to the obtained results, the size of γ′-precipitates does not significantly influence the affected volumes.

The Ni-based single crystal superalloy microstructure is recognizable by a standard γ/γ′ morphology. The face-centered cubic γ phase is essentially composed of Ni while the γ′ phase, with a cubic L12 crystal structure, is composed of Ni3(Al, Ti, Ta), subsequently approximated by Ni3Al. According to Ni-Al binary phase diagram, the melting temperature of the γ and γ′ phases are around 1455 °C and 1385 °C, respectively [54]. These disparities are controlled by the specific composition of each phase. Aluminum in the γ′-precipitates seems to decrease the melting temperature. Moreover, it is possible that the refractory elements added to strengthen the γ phase stability at high temperature [55–57], increasing its melting point. These local composition dissimilarities have a huge influence on the physical properties of the superalloys. For example, the incipient melting temperatures of AM1 and MC2 are around 1315 °C and 1330 °C, respectively, and closely linked to their respective compositions [58]. Finally, we wonder if the local differences of compositions could have an influence on the ablation kinetics.

Ma et al. have already compared the ablation regimes of CMSX-4, a second generation single crystal superalloy, pure nickel and the intermetallic Ni_3Al, by a femtosecond laser [37]. The pure nickel and Ni_3Al are representative of the γ and γ′ phases of nickel-based superalloys, respectively. First, it appears that less energy was required to ablate the superalloy compared to both other materials. In addition, slightly more energy was needed to ablate pure Ni than Ni_3Al. Nevertheless, the obtained values were very close, and the authors deduced that phase ablation within the superalloy by a femtosecond laser was uniform.

However, the ablation regimes of the materials are controlled by the laser pulse duration [38]. Thus, it is possible that the difference in optical and thermal properties of the γ and γ′ phases presents a more significant effect during nanosecond laser ablation.

Considering that both phases behaved distinctly during nanosecond laser ablation, the γ′ phase, with the lowest melting temperature, could melt and vaporize faster than the γ phase. This hypothesis seems consistent with the microstructure at the bottom of the textured holes. Indeed, as shown in Figure 14, it seems difficult to distinguish the γ′-precipitates (in dark gray) in the re-solidified area. In contrary, the matrix γ-lines (in light gray) are clearly identifiable. These two phases seem to behave very distinctly.

To understand the influence of the microstructure on the ablation mechanisms, both patterns were additionally textured on pure nickel, representative of the γ phase, and on a polycrystalline superalloy Inconel 718. Inconel 718 is a forged superalloy, enriched in niobium, which favors the precipitation of a γ′′ Ni_3Nb phase. This alloy is almost devoid of the γ′-precipitates (less than 5%). The main idea is to try to dissociate the individual impacts of γ and γ′ phases on the nanosecond laser ablation mechanisms.

Figure 16 shows patterns 1 and 2 textured on pure nickel, Inconel 718 and on AM1. It appears that pattern morphologies vary significantly between the pure nickel sample and the Ni-based superalloy ones. It seems that the laser intensity deposited on the surface to create pattern 1 ($8.8.10^{-2}$ GW/cm²) was not sufficient to ablate the pure nickel despite the thermal accumulation generated by the 50 laser pulses. However, with a higher laser intensity ($1.8.10^{-1}$ GW/cm² for pattern 2), the ablation of pure nickel could be initiated with

only 15 laser pulses. The patterns generated on the two nickel-based superalloys are similar.

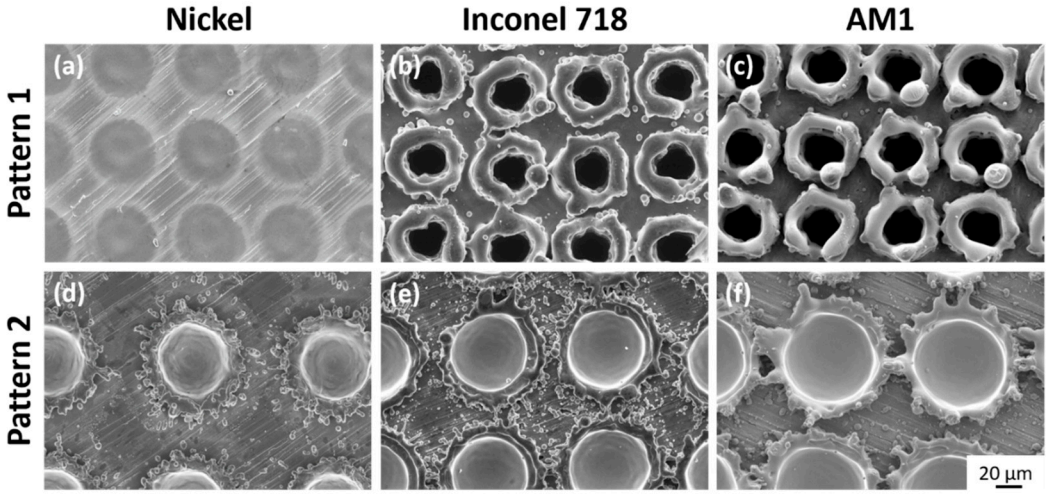

Figure 16. Patterns 1 textured on: (**a**) pure nickel, (**b**) Inconel 718, (**c**) AM1, and patterns 2 textured on: (**d**) pure nickel (**e**) Inconel 718, (**f**) AM1.

According to this hypothesis, it is relevant to observe a less ablated surface for the pure nickel than the AM1. Indeed, the γ phase is considered more resistant against nanosecond laser ablation than the γ'-precipitates. These results were in good agreement with those obtained by Ma et al. [37]. Nevertheless, dissimilarities between AM1 and Inconel 718, a material almost devoid of the γ' phase, were expected.

Figure 17 presents patterns generated under energetic conditions sufficient to deform the extreme surface of the impacted materials, but insufficient to generate material ejections. All the single crystal superalloys have a similar behavior, contrary to pure nickel and Inconel 718. Indeed, the surface of pure nickel does not appear to be marked with the same intensity as the other substrates. The geometry of pattern textured on the Inconel 718 and the induced oxidation mechanisms are also clearly different. It is possible to measure here an internal diameter of 34 µm for the Inconel 718, while it is equivalent to 44 µm for the other superalloys.

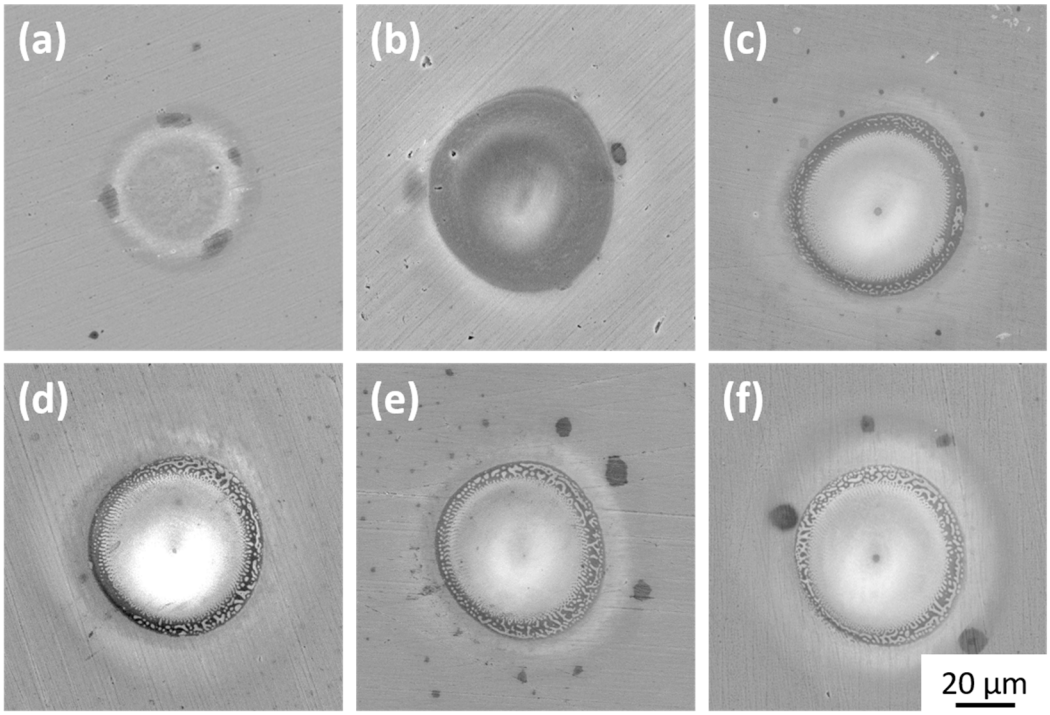

Figure 17. Patterns generated by low laser intensity on: (**a**) pure nickel, (**b**) Inconel 718, (**c**) MAR M200 + Hf + AgT, (**d**) MC2 + AgT, (**e**) AM1 + AgT and (**f**) CMSX-4 Plus + AgT.

Again, a difference in the ablation mechanisms of the γ and γ′ phases seems to be the most plausible hypothesis to explain these differences in ablation mechanisms. Consequently, the difference of thermal properties of the superalloy phases could have an impact on the measured thermally affected volumes, especially during the first steps of the laser ablation process. Under certain energetic conditions, superalloys could be considered as "composite" where the single-phase γ domain accentuates the resistance of the material during the laser ablation process.

With this hypothesis, it is possible to imagine that the differences in affected volumes observed for the same superalloys having different microstructures (same composition) are due to the different behaviors of the γ and γ′ phases. The additional heat treatments are known to optimize the size, distribution and volume fraction of γ′-precipitates [3]. Hence, the ablation would be accelerated by higher γ′ phase volume fractions, which could explain the fact that the thermally affected areas of the AM1 + AgT and CMSX-4 Plus + AgT are larger than the AM1 and CMSX-4 Plus ones. However, it is complicated to understand the behavior of MAR M200 + Hf, which is a very different alloy due to the presence of carbides.

Finally, additional efforts must be made to understand the differences between the considered superalloys. To this end, a detailed characterization of the material intrinsic properties and additional experiments to study the laser ablation mechanisms are necessary. However, despite the small differences observed in the thermally affected volumes, these studied patterns could be considered as equivalent whatever the analyzed Ni-based single crystal superalloys.

5. Conclusions

The following points summarize the content of this work:

- Infrared nanosecond laser ablation promotes the formation of asperities composed of melted, re-solidified matter around cavities. The microstructure within the asperities is clearly different from the core of superalloys. The standard γ/γ′ morphology cannot be observed.

- The morphology of asperity/superalloy junction has an influence on the asperity cooling phenomena and, consequently, on the recrystallization mechanisms. Indeed, an important junction favors an epitaxial growth of the asperities with the substrate. On the contrary, a small junction promotes the formation of recrystallized asperities.
- Whatever the considered Ni-based single crystal superalloys, textured patterns including thermally affected volumes are quite similar. However, regarding thermal-affected volumes, slight dissimilarities were noticed between the same superalloys but having different microstructures.
- During infrared nanosecond laser ablation, Ni-based single crystal superalloys could be considered as "composite" with a γ phase more resistant to the ablation than γ'-precipitates. The local competition of melting and vaporization kinetics could explain the obtained thermal-affected volumes.

Author Contributions: This article is the result of a collective work by all the authors mentioned in the framework of the Ph.D. thesis of L.D. and supervised by S.C., J.C. and R.C. Conceptualization, S.C., J.C. and R.C.; methodology, L.D, S.C., J.C., P.V. and R.C.; validation, S.C., J.C. and R.C.; formal analysis, L.D and S.C.; investigation, L.D.; resources, L.D, S.C., J.C. and P.V.; data curation, L.D, S.C., J.C., P.V. and R.C.; writing—original draft preparation, L.D. and S.C.; writing—review and editing, L.D and S.C.; visualization, L.D, S.C., J.C., P.V. and R.C.; supervision, L.D, S.C., J.C., P.V. and R.C.; project administration, S.C., J.C., and R.C.; funding acquisition, S.C., J.C., and R.C. All authors have read and agreed to the published version of the manuscript.

Funding: The authors gratefully acknowledge SAFRAN Tech for the financial support of this study. As well, CPER and FEDER (Poitou-Charentes Region, Vienne Department, European Community, Poitiers Agglomeration and French Education and Research Ministry) financial supports are gratefully acknowledged.

Institutional Review Board Statement: Not applicable.

Informed Consent Statement: Not applicable.

Data Availability Statement: This work is the result of the Ph.D. work of Lucille Despres which was carried out within the framework of an industrial thesis at the request of the company SAFRAN Tech. This thesis was defended in December 2020 and is entitled: Thermomechanical fatigue behavior at high temperature of a laser textured thermal barrier system. Discipline: Materials. University of Burgundy Franche-Comté, 2020. French. (NNT: 2020UBFCA030; tel-03164978v1).

Acknowledgments: The authors gratefully acknowledge SAFRAN Tech for the financial support of this study. As well, CPER and FEDER (Poitou-Charentes Region, Vienne Department, European Community, Poitiers Agglomeration and French Education and Research Ministry) financial supports are gratefully acknowledged. Moreover, it is within the framework of a collaboration with the laboratory PIMM of the ENSAM of Paris that the measurements of the coefficient of absorption of materials could be carried out. We would like to thank the colleagues involved (Frederic Coste). ICB is supported by the EUR-EIPHI Graduate School (grant no. 17-EURE-0002).

Conflicts of Interest: The authors declare no conflict of interest.

References

1. Campbell, D.J. Advanced aero-engine concepts controls. In *Advanced Aero-Engine Concepts and Controls*; AGARD: Neuilly sur Seine, France, 1996.
2. Delcourt, O. Les défits matériaux et procédés pour les équipements aéronautiques. In Proceeding of the Conférence A3TS, 2016. Available online: https://www.mediachimie.org/sites/default/files/Espace_p117.pdf (accessed on 29 October 2021)
3. Reed, R.C. *The Superalloys—Fundamentals and Applications*; Cambridge University Press: Cambridge, UK, 2008.
4. Paquin, S.; Cariou, R. Turbine Blade Having an Improved Structure. Patent WO 2018/189434A2, 18 October 2018.
5. Rollinger, A.; Cariou, R.; Flamme, T.; Paquin, S. Turbine Blade Comprising a Cooling Circuit. Patent WO 2018/060627 A1, 5 October 2017.
6. Levi, C.G.; Hutchinson, J.W.; Vidal-Sétif, M.H.; Johnson, C.A., Environmental degradation of thermal-barrier coatings by molten deposits. *MRS Bull.* **2012**, *37*, 932–941.
7. Evans, A.G.; Mumm, D.R.; Hutchinson, J.W.; Meier, G.H.; Pettit, F.S. Mechanisms controlling the durability of Thermal Barrier Coatings. *Progr. Mater. Sci.* **2001**, *46*, 505–553.

8. Evans, H.E. Oxidation failure of TBC systems: An assessment of mechanisms. *Surf. Coat. Technol.* **2011**, *206*, 1512–1521.
9. Dryepondt, S.; Porter, J.R.; Clarke, D.R. On the initiation of cyclic oxidation-induced rumpling of platinum-modified nickel aluminide coatings. *Acta Mater.* **2009**, *57*, 1717–1723.
10. Giggins, C.S.; Kear, B.H.; Pettit, F.S.; Tien, J.K. Factors Affecting Adhesion of Oxide Scales on Alloys. *Metall. Trans.* **1974**, *5*, 1685–1688.
11. Evans, H.E. Modelling oxide spallation. *Mater. High Temp.* **1994**, *12*, 219–227.
12. Tolpygo, V.K.; Clarke, D.R. On the rumpling mechanism in nickel-aluminide coatings part II: Characterization of surface undulations and bond coat swelling. *Acta Mater.* **2004**, *52*, 5129–5141.
13. Tolpygo, V.K.; Clarke, D.R. Surface rumpling of a (Ni, Pt)Al bond coat induced by cyclic oxidation. *Acta Mater.* **2000**, *48*, 3283–3293.
14. Tolpygo, V.K.; Clarke, D.R.; Murphy, K.S. Oxidation-induced failure of EB-PVD thermal barrier coatings. *Surf. Coat. Technol.* **2001**, *146–147*, 124–131.
15. Spitsberg, I.T.; Mumm, D.R.; Evans, A.G. On the failure mechanisms of thermal barrier coatings with diffusion aluminide bond coatings. *Mater. Sci. Eng. A* **2005**, *394*, 176–191.
16. Zhao, H.; Yu, Z.; Wadley, H.N.G. The influence of coating compliance on the delamination of thermal barrier coatings. *Surf. Coat. Technol.* **2010**, *204*, 2432–2441.
17. Kromer, R. *Etude des Effets des Préparations de Surface Avant Projection Thermique—Application à un Système Barrière Thermique*; Université de Technologie de Belfort-Montbéliard: Sevenans, France, 2016.
18. Kromer, R.; Cormier, J.; Costil, S.; Courapied, D.; Berthe, L.; Peyre, P. High temperature durability of a bond-coatless plasma-sprayed thermal barrier coating system with laser textured Ni-based single crystal substrate. *Surf. Coat. Technol.* **2018**, *337*, 168–176.
19. Kromer, R.; Mauget, F.; Despres, L.; Costil, S.; Cormier, J. Thermo-mechanical fatigue evaluation of a thermal barrier coating bond-coatless system. *Mater. Sci. Eng. A* **2019**, *756*, 130–141.
20. Aufray, M. Fascicule : Adhésion et Adhérence des Matériaux. 2009. Available online: http://maelenn.aufray.free.fr/cours/fascicule-cours-adhesion-site-web.pdf (accessed on).
21. McBain, J.W.; Hopkins, D.G. On Adhesives and Adhesive Action. *J. Phys. Chem.* **1925**, *29*, 188–204.
22. Garcia-Alonso, D.; Serres, N.; Demian, C.; Costil, S.; Langlade, C.; Coddet, C. Pre-/during-/post-laser processes to enhance the adhesion and mechanical properties of thermal-sprayed coatings with a reduced environmental impact. *J. Therm. Spray Technol.* **2011**, *20*, 719–735.
23. Neves, D.; Diniz, A.E.; de Lima, M.S.F. Efficiency of the laser texturing on the adhesion of the coated twist drills. *J. Mater. Process. Technol.* **2006**, *179*, 139–145.
24. Kromer, R.; Costil, S.; Cormier, J.; Courapied, D.; Berthe, L.; Peyre, P.; Boustie, M. Laser surface patterning to enhance adhesion of plasma sprayed coatings. *Surf. Coat. Technol.* **2015**, *278*, 171–182.
25. Courapied, D.; Kromer, R.; Berthe, L.; Peyre, P., Costil, S.; Cormier, J.; Boustie, M.; Milhet, X. Laser adhesion test for thermal sprayed coatings on textured surface by laser. *J. Laser Appl.* **2016**, *28*, 022509.
26. Kromer, R.; Costil, S.; Cormier, J.; Berthe, L.; Peyre, P.; Courapied, D. Laser Patterning Pretreatment before Thermal Spraying: A Technique to Adapt and Control the Surface Topography to Thermomechanical Loading and Materials. *J. Therm. Spray Technol.* **2016**, *25*, 401–410.
27. Kromer, R.; Danlos, Y.; Aubignat, E.; Verdy, C.; Costil, S. Coating deposition and adhesion enhancements by laser surface texturing—metallic particles on different classes of substrates in cold spraying process. *Mater. Manuf. Process.* **2017**, *32*, 1642–1652.
28. Pollock, T.M.; Tin, S. Nickel-based surperalloys for advanced turbine engines: Chemistry, microstructure, and properties. *J. Propuls. Power* **2006**, *22*, 361–374.
29. Wahl, J.B.; Harris, K. *Improved 3rd Generation Single Crystal Superalloy CMSX-4® Plus (SLS)—A Study of Evolutionary Alloy Development*; Cannon-Muskegon: Muskegon, MI, USA, 1984.
30. Tin, S.; Pollock, T.M. Phase instabilities and carbon additions in single-crystal nickel-base superalloys. *Mater. Sci. Eng. A* **2003**, *348*, 111–121.
31. Rame, J.; Utada, S.; Bortoluci Ormastroni, L.; Mataveli Suave, L.; Menou, E.; Despres, L.; Kontis, P.; Cormier, J. Platinum containing new generation nickel-based superalloy for single crystalline applications. In *Superalloys 2020 TMS*; Springer: Cham, Switzerland, 2020; pp. 71–81.
32. Semaltianos, N.G.; Perris, W.; Cheng, J.; French, P.; Sharp, M.; Dearden, G.; Watkins, K.G. Picosecond laser ablation of nickel-based superalloy C263. *Appl. Phys. A* **2010**, *98*, 345–355.
33. Semaltianos, N.G.; Perris, W.; French, P.; Sharp, M.; Dearden, G.; Logothetidis, S.; Watkins, K.G. Femtosecond laser ablation characteristics of nickel-based superalloy C263. *Appl. Phys. A* **2009**, *94*, 999–1009.
34. McDonald, J.P.; Ma, S.; Pollock, T.M.; Yalisove, S.M.; Nees, J.A. Femtosecond pulsed laser ablation dynamics and ablation morphology of nickel based superalloy CMSX-4. *J. Appl. Phys.* **2008**, *103*, 1–8.
35. Petronic, S.; Drecun-Nesic, S.; Milosavljevic, A.; Sedmak, A.; Popovic, M.; Kovacevic, A. Microstructure changes of nickel-base superalloys induced by Interaction with femtosecond laser beam. *Acta Phys. Pol. A* **2009**, *116*, 550–552.
36. Ma, S.; McDonald, J.P.; Tryon, B.; Yalisove, S.M.; Pollock, T.M. Femtosecond laser ablation regimes in a single-crystal superalloy. *Metall. Mater. Trans. A* **2007**, *38*, 2349–2357.
37. Chichkov, B.N.; Momma, C.; Nolte, S.; Alvensleben, F.v.; Tünnermann, A. Femtosecond, picosecond and nanosecond laser ablation of solids. *Appl. Phys. A* **1996**, *63*, 109–115.

38. Zeng, X.; Mao, X.; Greif, R.; Russo, R.E. Experimental investigation of ablation efficiency and plasma expansion during femto-second and nanosecond laser ablation of silicon. *Appl. Phys. A* **2005**, *80*, 237–241.
39. Costil, S.; Despres, L.; Cormier, J.; Mauget, F.; Cariou, R.; Joulia, A.; Saboundji, A.; Mataveli Suave, L. Laser surface texturing to imporve EB-PVD thermal barrier coating adhesion. In Proceedings of the ITSC, Quebec, Canada, 24–28 May 2021.
40. Grosdidier, T.; Hazotte, A.; Simon, A. Precipitation and dissolution processes in γ/γ′ single crystal nickel-based superalloys *Mater. Sci. Eng. A* **1998**, *256*, 183–196.
41. Costil, S.; Lamraoui, A.; Langlade, C.; Heintz, O.; Oltra, R. Surface modifications induced by pulsed-laser texturing—Influence of laser impact on the surface properties. *Appl. Surf. Sci.* **2014**, *288*, 542–549.
42. Kato, T.; Kobayashi, T.; Nikov, R.G.; Nedyalkov, N.N.; Atanasov, P.A. Surface modification of Ti6Al4V by nanosecond laser ablation for biomedical applications. *J. Phys. Conf. Ser.* **2015**, *605*, 012022.
43. Kurella, A.; Dahotre, N.B. Review paper: Surface Modification for Bioimplants: The Role of Laser Surface. *J. Biomater. Appl.* **2005**, *20*, 1–25.
44. Jouvard, J.M.; Soveja, A.; Pierron, N.; Fonderie, D.; Creusot, L. Thermal modelling of metal surface texturing by pulsed laser. In Proceedings of the COMSOL Users Conference, Paris, France, 7 November 2006.
45. Semak, V.V.; Hopkins, J.A.; Mccay, M.H.; Mccay, T.D. A concept for a hydrodynamic model of keyhole formation and support during laser welding. *ICALEO* **1994**, 641–650.
46. Semak, V.; A. Matsunawa, A. The role of recoil pressure in energy balance during laser materials processing. *J. Phys. D Appl. Phys.* **1997**, *30*, 2541–2552.
47. Soveja, A.; Jouvard, J.M.; Grevey, D. Metal Surface Laser Texturing: Multiphysics Modelling of a Single Impact Effect. In Proceedings of the COMSOL Users Conference, Grenoble, France, 23–24 October 2007.
48. Leitz, K.; Redlingshöfer, B.; Reg, Y.; Otto, A.; Schmidt, M. Metal Ablation with Short and Ultrashort Laser Pulses. *Physics Proc.* **2011**, *12*, 230–238.
49. Bäuerle, D. *Laser Processing and Chemistry*, 4th ed.; Springer: Berlin/Heidelberg, Germany, 2011.
50. Allmen, M.v.; Blatter, A. *Laser-Beam Interactions with Materials*, 2nd ed.; Springer: Berlin/Heidelberg, Germany, 1998.
51. Acharya, M.V.; Fuchs, G.E. The effect of long-term thermal exposures on the microstructure and properties of CMSX-10 single crystal Ni-base superalloys. *Mater. Sci. Eng. A* **2004**, *381*, 143–153.
52. Wu, J.; Jiang, X.; Wang, Y.; Dong, J.; Lou, L. Effects of Ta on microstructure stability and mechanical properties of hot corrosion resistant Ni-based single crystal superalloys during long-term thermal exposure, *Mater. Sci. Eng. A* **2021**, *806*, 140829.
53. Steuer, S.; Hervier, Z.; Thabart, S.; Castaing, C.; Pollock, T.M.; Cormier, J. Creep behavior under isothermal and non-isothermal conditions of AM3 single crystal superalloy for different solutioning cooling rates. *Mater. Sci. Eng. A* **2014**, *601*, 145–152.
54. Selezneff, S. *Etude et Développement de Revêtements Gamma-Gamma' Riches en Platine, Elaborés par Spark Plasma Sintering (SPS)*; Application au Système Barrière Thermique; Université de Toulouse: Toulouse, France, 2011.
55. Giamei, A.F.; Anton, D.L. Rhenium additions to a Ni-base superalloy: Effects on microstructure. *Metall. Mater. Trans. A* **1985**, *16*, 1997–2005.
56. Caron, P.; Khan, T. Evolution of Ni-based superalloys for single crystal gas turbine blade applications. *Aerosp. Sci. Technol.* **1999**, *3*, 513–523.
57. Durrand-Charre, M. *The Microstructure of Superalloys*; CRC Press: Boca Raton, FL, USA, 2000.
58. Caron, P.; Khan, T. Improvement of creep strength in a nickel-base single-crystal superalloy by heat treatment. *Mater. Sci. Eng.* **1983**, *61*, 173–184.